2nd Advanced Optical Metrology Compendium

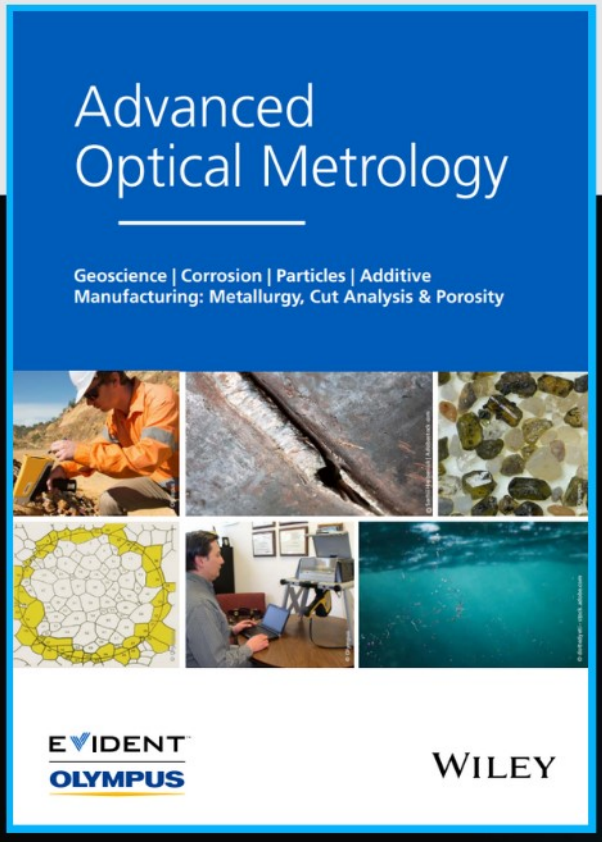

The latest eBook from Advanced Optical Metrology. Download for free.

This compendium includes a collection of optical metrology papers, a repository of teaching materials, and instructions on how to publish scientific achievements.

With the aim of improving communication between fundamental research and industrial applications in the field of optical metrology we have collected and organized existing information and made it more accessible and useful for researchers and practitioners.

EVIDENT
OLYMPUS

WILEY

ADVANCED FUNCTIONAL MATERIALS
www.afm-journal.de

Direct Freeform Laser Fabrication of 3D Conformable Electronics

Bujingda Zheng, Ganggang Zhao, Zheng Yan, Yunchao Xie, and Jian Lin**

3D conformable electronic devices on freeform surfaces show superior performance to the conventional, planar ones. They represent a trend of future electronics and have witnessed exponential growth in various applications. However, their potential is largely limited by a lack of sophisticated fabrication techniques. To tackle this challenge, a new direct freeform laser (DFL) fabrication method enabled by a 5-axis laser processing platform for directly fabricating 3D conformable electronics on targeted arbitrary surfaces is reported. Accordingly, representative laser-induced graphene (LIG), metals, and metal oxides are successfully fabricated as high-performance sensing and electrode materials from different material precursors on various types of substrates for applications in temperature/light/gas sensing, energy storage, and printed circuit board for circuit. Last but not the least, to demonstrate an application in smart homes, LIG-based conformable strain sensors are fabricated and distributed in designated locations of an artificial tree. The distributed sensors have the capability of monitoring the wind speed and direction with the assistance of well-trained machine-learning models. This novel process will pave a new and general route to fabricating 3D conformable electronic devices, thus creating new opportunities in robotics, biomedical sensing, structural health, environmental monitoring, and Internet of Things applications.

1. Introduction

3D conformable electronics with fundamentally new characteristics and functionalities have shown promising applications in various fields including epidermal electronics, bio-integrated electronics, conformable circuits/display, structural health monitoring, wearable sensors, tactile sensors, and deformable optoelectronics.[1] These applications would be mostly impossible by the conventional planar electronics. In the early days, well-established planar microfabrication techniques were widely applied for fabricating 3D electronics on flexible and stretchable substrates. The process involves two key steps, patterning electronics on planar, rigid, and brittle substrates such as silicon wafers and glass plates followed by transferring them onto the curvilinear surfaces. The inherently 2D planar nature makes it intrinsically incompatible for fabricating 3D conformable electronics onto the complex, curvilinear surfaces such as living organisms and curved focal planes. Moreover, insufficient interface between sensors and the targeted surfaces results in difficulty in collection of signals from the surrounding physical world. Hence, researchers have tried to develop novel and versatile fabrication techniques to meet the increasingly stringent design constraints from arbitrary 3D surfaces with complex topographies.

In the past two decades, impressive technical advances have overcome many of the drawbacks of the traditional planar electronics fabrication techniques. They include bulk micromachining, aerosol jet/hybrid 3D printing,[2] molding,[3] photonic sintering,[4] and stress-induced assembly methods.[5] After the device fabrication, they are then transferred onto the rigid, deformable, or/and time-dynamic curvilinear surfaces by a variety of techniques including transfer printing,[6] thermo- and vacuum-forming,[7] and hydro-printing.[8] However, these processes suffer from the need of many fabrication steps, limitation in available materials, mechanical mismatch between electronics and surfaces, high capital investment, and low agility, thus hindering their widespread applications. Recently, intense pulsed light-induced transfer[9] and temporary drawn-on-skin transfer[10] methods were developed to fabricate 3D conformable electronics. But both methods show disadvantages of requiring photomasks and low positioning accuracy when transferring the patterns from the masks onto targeted locations of the complex 3D surfaces. In addition, they can only handle limited types of materials, such as materials with lower evaporating point and strong adhesive ability, and require the post-processing steps. Hence, it is still quite desired to develop advanced fabrication methods that feature fewer processing steps, enable to process more accessible materials, and result in easier and faster device assembly.

Recently, direct laser writing (DLW), a maskless, rapid fabrication technique, has been successfully demonstrated to efficiently fabricate a wide range of materials including

B. Zheng, G. Zhao, Z. Yan, Y. Xie, J. Lin
Department of Mechanical and Aerospace Engineering
University of Missouri
Columbia, MO 65201, USA
E-mail: yxpx3@umsystem.edu; linjian@missouri.edu
Z. Yan
Depeartment of Biomedical
Biological, and Chemical Engineering
University of Missouri
Columbia, MO 65201, USA
The ORCID identification number(s) for the author(s) of this article can be found under https://doi.org/10.1002/adfm.202210084.

DOI: 10.1002/adfm.202210084

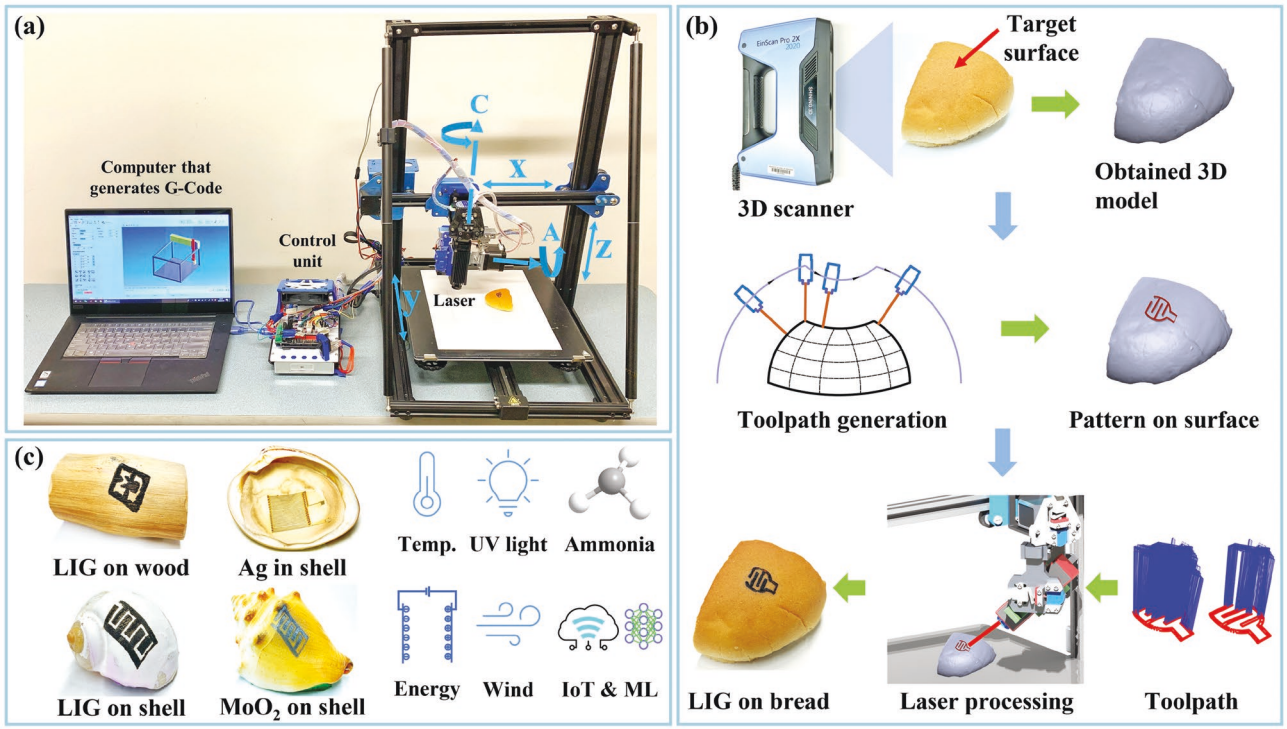

Figure 1. System and workflow of a DFL processing technique for fabricating 3D conformable devices. a) A photograph of the 5-axis laser processing apparatus showing three main systems. b) Workflow of fabricating 3D conformable electronics using a 3D scanner and the 5-axis laser processing apparatus. c) Figures and schematic summarizing examples of processed LIG, Ag, and MoO_2 materials from different precursors on various substrates as well as their versatile applications in sensing and energy storage.

laser-induced graphene (LIG),[11] metal and alloys, and metal oxides/sulfides, creating many opportunities for applications in sensors,[12] energy storage and conversion,[13] and soft actuators.[14] However, the mainstream DLW is operated on planar surfaces enabled by an apparatus with two actuation axes with only two degrees of freedom (DOF). Thus, to realize 3D conformable electronics, transferring the fabricated electrodes or/and sensors onto the targeted curvilinear surfaces is still required.[12a] This additional transferring process inherits the same issue that the positioning accuracy or conformability of the transferred devices to the curvilinear surfaces cannot be fully guaranteed. Therefore, advancing the existing DLW technique with improved agility for 3D conformable electronics fabrication is much needed while it is still a challenge. Herein, we demonstrate a direct freeform laser (DFL) fabrication technique enabled by a 5-axis laser processing platform to directly fabricate 3D conformable electronics on arbitrary curvilinear surfaces with complex topographies (**Figure 1**). Compared with the traditional 3-axis laser apparatus, the two added axes enable rotation motions of the laser beam, thus ensuring the laser beam perpendicular to the targeted curvilinear surface while keeping a constant focus independent of surface topographies. In addition, we demonstrated its capability of processing various types of functional materials (LIG, metal, and metal oxides) conformably on different types of material surfaces (wood, bread, polymer, shell, and rock) from different precursors. These functioning materials show applications in temperature, UV light, and ammonia (NH_3) sensing, energy storage, and printed circuit board (PCB) for an internet-of-thing (IoT) circuit consisting of microcontroller, and light-emitting diode (LED). Finally, the LIG-based strain sensors were conformably fabricated on tws of an artificial tree for indoor ventilation monitoring. These sensors can automatically detect the wind direction and speed with the integrated machine learning (ML) algorithms, showing capability of the tree being a smart decorator at home.

The advantages of the proposed DFL fabrication technique can be summarized as follows: (i) omitting the transferring steps for fabricating conformable electronics; (ii) enabling easy and accurate positioning of the fabricated 3D electronics to the targeted locations of the arbitrary surfaces with complex topographies; (iii) enabling to process many types of materials with consistent quality on the curvilinear surfaces; and (iv) creating good interfaces between the fabricated materials and the targeted surfaces. This novel process will pave a new route to fabricating 3D conformable electronic devices, which can be better integrated with the surroundings to collect data that is mostly inaccessible or difficultly secured by other planar devices. Thus, it will create new opportunities in robotics, biomedical sensing, structural health, environmental monitoring, and IoT applications.

2. Results and Discussion

Figure 1a shows a photograph of the 5-axis DFL processing platform. It features motion, lasing, and control systems. The motion system contains three linear gantries (X, Y, and Z) and

two additional rotary axes (A and C) for five DOF actuation. The two rotational motions are driven by two separate motors (Figure S1, Supporting Information). The laser is installed on a stage directly connected A-axis actuator. It has a wavelength of 450 nm and a tunable power maximized at 5.5 W (Figure S2, Supporting Information). Irradiated on the targeted free-form surfaces, it can convert various material precursors to functional materials with pre-designed patterns. The control system consists of an Arduino Mega 2560 R3 and a RAMPS 1.6 plus board. They execute the G-code command output from LinuxCNC which generates the toolpath of the laser beam. The toolpath can keep the laser beam perpendicular to the targeted surfaces with a constant laser focus while scribing the designed device patterns. Figure 1b illustrates the flowchart of fabricating 3D conformable electronics on an exemplary surface using the DFL technique. First, a specimen, e.g., a piece of bread, with a curvilinear surface is placed on a turntable. Its 3D coordinates are collected using a structured light 3D scanner (Figure S3, Supporting Information). Then the collected coordinate data forms a 3D mesh model which is then reconstructed to a 3D solid model in SOLIDWORKS (Figure S4a,b, Supporting Information). Then, a pre-designed pattern is projected onto the curvilinear surface of the solid model (Figure S4b, Supporting Information). The toolpath for fabricating the pattern is first generated in the coordinate system of the part by LinuxCNC (Figure S4c, Supporting Information). It is then transformed into the machine coordinate system of our platform through MATLAB (Figure S4, Supporting Information). The toolpath contains serials of G-codes to control the motions of the five axes of the DLF apparatus and the laser parameters, e.g., laser powers and scanning rates. After aligning the laser spot to the right initial position of the specimen placed on the working platform (Figure S4d, Supporting Information), the control unit actuates axes to make the laser beam follow the toolpath of the predesigned pattern. Video S1 (Supporting Information) shows fabrication of a LIG pattern directly from the surface of the bread. Besides, it is demonstrated that the DFL technique can fabricate LIG from natural wood, polyimide (PI), and polyvinylidene fluoride (PVDF) as well as producing metals such as Ag, and metal oxides such as MoO_2 on various types of surfaces (Figure 1c). The proposed formation mechanism of LIG from PVDF, Ag, and MoO_2 can be found in Figure S5–S7 (Supporting Information), respectively. The laser processing procedures with optimal parameters for fabricating various materials were summarized in Table S1 (Supporting Information). These easily accessible materials can be readily applied for 3D conformable devices including temperature, UV light, and ammonia sensors, supercapacitors, printed circuit board, and strain sensors for smart IoT furniture (Figure 1c).

The demonstrated 5-axis laser processing apparatus is superior to the traditional 3-axis one in the following aspects. First, the laser beam driven by only three axes cannot reach surfaces that form angles of > = 180° with the laser beam (**Figure 2**a), while a 5-axis laser can easily deal with this situation (Figure 2b). Figure 2c validates the hypothesis. The LIG fabricated by the 5-axis laser is continuous, while the one fabricated by the 3-axis laser is discontinuous on the surface that is parallel to the laser beam. Second, in comparison with the 3-axis laser apparatus, the 5-axis one can keep the laser beam perpendicular to the tangent planes of the surfaces with various topographies. Such advantages make DFL superior to recent emerging 3D printing techniques,[2b,c] as an extrusion nuzzle of a 3D printer cannot keep perpendicular to the curvilinear surfaces. Third, in the 5-axis laser apparatus, the laser focus length can be kept constant when the laser beam scribes the curvilinear surfaces (Figure 2d), thus helping to afford materials with improved consistency in quality. We systematically investigated the effect of the focus distance of the laser beam on the pattern resolution and sheet resistance of LIG (Figure S8 and S9, Supporting Information). As shown in Figure S8 (Supporting Information), when the laser is focused, linewidth of the LIG strip is 179 μm, while the linewidths vary from 221 to 114 μm when the defocusing distances are changed from −4 to 5 mm. Figure S9 (Supporting Information) reveals that defocusing leads to an increase of sheet resistance of LIG. When the laser is focused, LIG shows the smallest sheet resistance of 345 Ω sq^{-1}. It is dramatically increased by 426% to 1808 Ω sq^{-1} when the defocusing distance increases to 4 mm. These results further validate the advantage of our 5-axis laser processing apparatus in maintaining constant laser focus to target surfaces.

During the implementation, it is found that a fixed laser power and a scanning rate may result in non-uniform laser flux along the scribed curvilinear surfaces. It is well-known that smooth changes of tool orientation can improve both kinematics performance of the AC axes and surface quality of machined parts.[15] This requires a slower motion speed of the AC axes than those of the XYZ axes, resulting in longer manufacturing time in some regions, e.g., a curvilinear surface, than the flat surfaces. In our case, with a constant laser power and a scanning rate, a laser flux irradiated on a curvilinear surface would be larger than the one on a flat surface or a surface with a smaller curvature. This uneven laser irradiation to the precursors may result in non-uniform material quality, which is validated by the result shown in Figure S10a (Supporting Information). Hence, to achieve a constant laser flux along different regions of a curvilinear surface, the laser power is dynamically scaled from the designated value with the scanning speed. As a comparison, the LIG fabricated by a laser with dynamic powers is more uniform (Figure S10b, Supporting Information). Unless specified, all the following samples were fabricated using dynamically tuned laser powers.

To quantify the quality of the as-synthesized LIG, their Raman spectra and sheet resistance (R_S) were measured on six different positions along the curvilinear surfaces. Here, LIG was directly patterned on PI films attached to the spherical surfaces with a radius of 32.5 mm (Figure 2d). As an indicator of pattern resolution, the minimum linewidth of LIG was determined to be 109 μm (Figure S11, Supporting Information). A total of 572 Raman spectra were collected from LIG at six different positions along the surfaces of five different samples (Figure S12, Supporting Information). They all show three characteristic peaks at ≈1330, ≈1580, and ≈2700 cm^{-1}, corresponding to the D, G, and 2D bands of a graphitic material (Figure 2e).[11,16] The calculated I_G/I_D ratios of LIG at six positions are all close to 1.0, indicating a low level of defects in LIG (upper panel of Figure 2f). Crystallinity sizes (L_a, nm) along with a axis of LIG were calculated from the I_G/I_D ratios. They are close to 40 nm for LIG at all six positions (lower panel

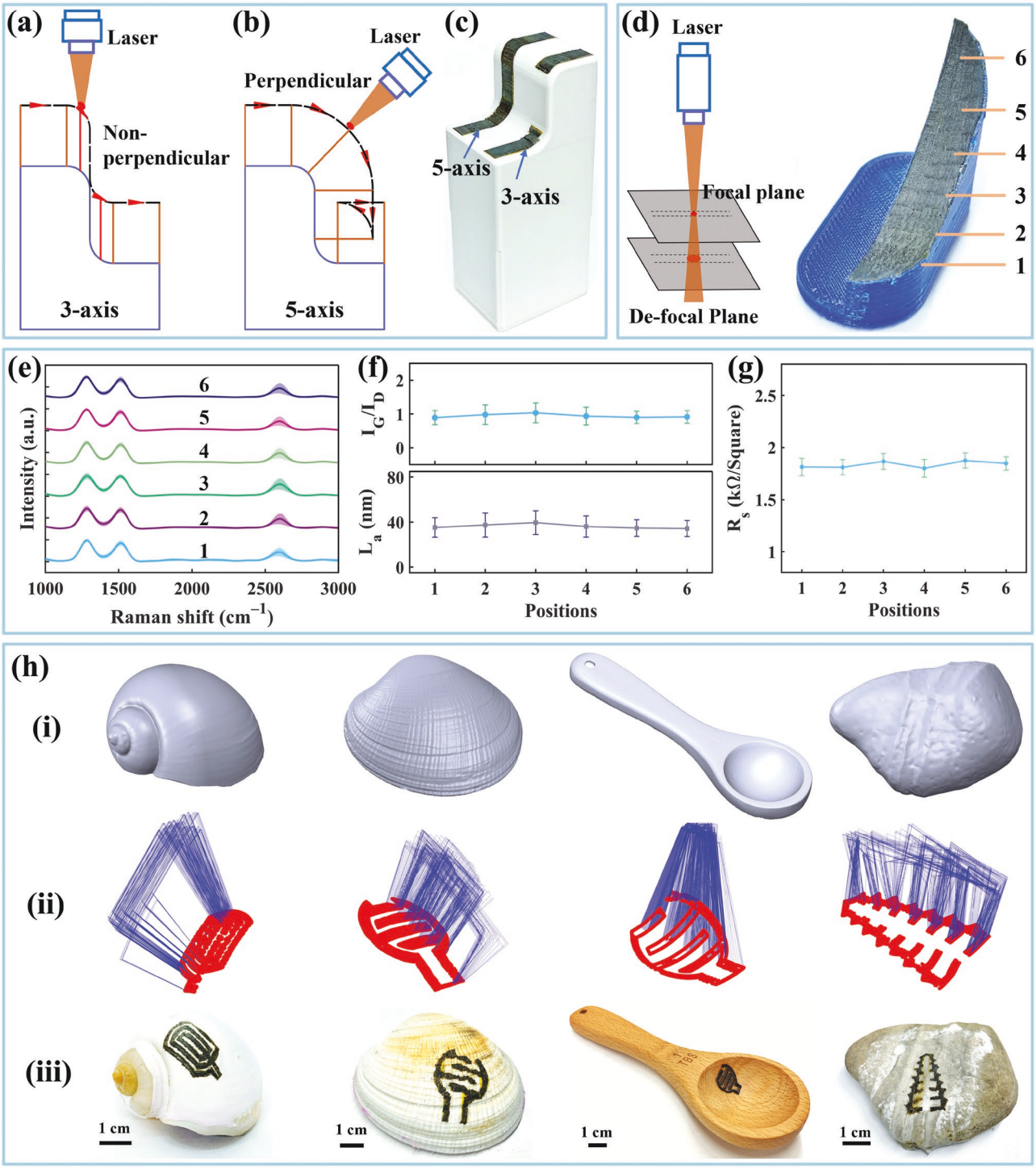

Figure 2. Performance of the 5-axis DLF technique in processing LIG on various surfaces. Schematic toolpaths of a 3-axis laser (a) and a 5-axis laser (b) along a curvilinear surface. c) A photograph of two LIG strips fabricated by a 3-axis laser and a 5-axis laser apparatus. d) Schematic of focal and de-focal laser planes and a photograph of LIG fabricated along a spherical surface. e) Raman spectra of LIG measured at six different positions on the surface shown in (d). f) Statistic analysis on the ratios of I_G/I_D (upper panel) and calculated average LIG domain sizes (lower panel) at six different positions shown in (d). g) Sheet resistance (*R*s) of LIG measured at six different positions on the surface shown in d. h) LIG fabricated on surfaces of moon snail shell, clamshell, wood spoon, and stone: i) 3D scanned solid models; ii) toolpaths to fabricate patterns on the targeted surfaces; iii) photographs of conformable LIG patterns fabricated on these surfaces.

of Figure 2f). Their sheet resistances (R_S) are statistically the same, showing average values of <2000 Ω sq^{-1} (Figure 2g). To test conformability of LIG on the surfaces, the LIG strips with the same effective lengths and widths were fabricated on surfaces with different curvatures (Figure S13a,b, Supporting Information). Figure S13c (Supporting Information) shows that

their electrical resistances exhibit statistically the same values. These characterization results demonstrate the uniform and high quality of LIG fabricated by our 5-axis DFL apparatus. As shown in Figure S14 (Supporting Information), LIG is porous, which agrees well with the previous studies.[14] Moreover, the versatility of the DFL technique was demonstrated by its ability to process and pattern materials on arbitrary complex surfaces on subjects such as a convex moon snail shell, a convex rugged clamshell surface, a concave wood spoon, and a rugged stone. 3D scanned models of the objects, toolpaths to project the patterns to the targeted surfaces, and the resulting LIG on these surfaces are shown in Figure 2h(i–iii), respectively. It is worth mentioning that the LIG patterns on moon snail shell, clamshell, and stone were processed from PVDF coated on their surfaces, while the one inside the wood spoon surface was directly scribed from the wood.

In addition to LIG, metal and metal oxides can be also fabricated by the DFL technique. As examples, sliver (Ag)[17] and molybdenum oxide (MnO_2)[18] were processed and patterned on surfaces of the clamshell, Florida fighting conch shell, and moon snail shell as conformable sensing materials for temperature, UV irradiation, and NH_3 detection (**Figure 3**). A comparison on the sensing performances of these conformable sensors fabricated by the DFL technique with those in the recently published work is summarized in Table S2 (Supporting Information). They show either comparable or superior performance. All sensing performances were evaluated using the ratio of electrical resistance change, as described by $\Delta R/R_0 = (R - R_0)/R_0$, where R and R_0 are the resistance before and after exposure to an external stimulus, respectively. Temperature sensors are useful in health monitoring, home appliance, manufacturing industry, and environmental inspection.[19] To detect the temperature stimulus, Ag electrodes with a thickness of 0.05 mm were synthesized and patterned on a concave surface of a clamshell from a precursor of silver citrate precipitate (Figure 3a,b). The minimum linewidth of Ag was shown to be 111 µm (Figure S15, Supporting Information). Raman spectra show characteristic peaks centered at 241 cm^{-1} (Figure S16, Supporting Information), assigning to the Ag-O stretching mode.[17] Scanning electron microscopy (SEM) images show that the fabricated Ag exhibits bulk morphology (Figure S17, Supporting Information). Owing to its high flexibility and high current levels with acceptable sensitivity,[20] Ag has been widely used as a soft thermistor. It exhibits a positive temperature coefficient (PTC), i.e., the resistance linearly increases with the temperature rise, which is validated in Figure 3c. The correlation between $\Delta R/R_0$

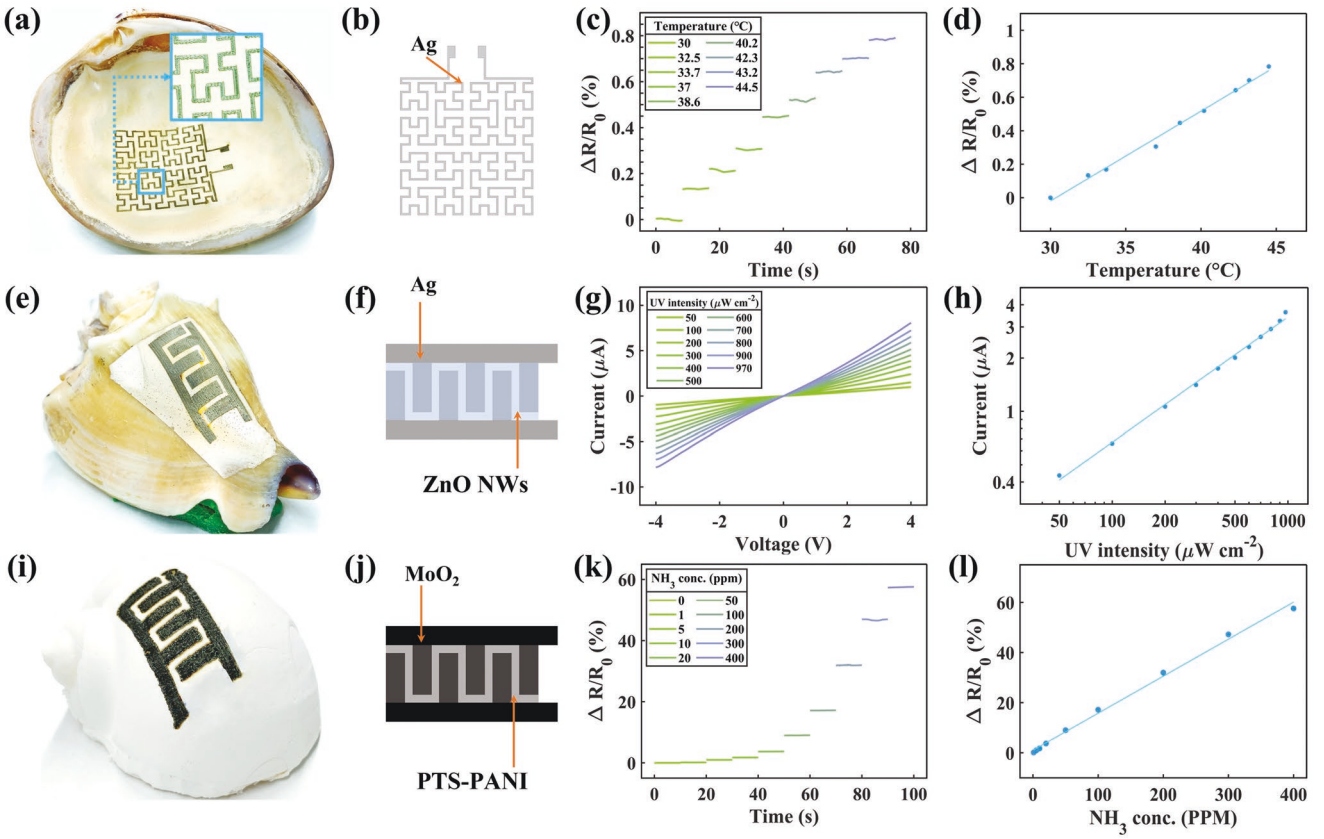

Figure 3. Performance of three 3D conformable sensors for temperature, UV light, and ammonia sensing. a) A photograph of an Ag electrode patterned on a concave surface of a clam. b) Schematic of the Ag Hilbert pattern. c) Dynamic resistance response of an Ag electrode to different temperatures. d) Resistance changes of an Ag electrode as a function of temperature. e) A photograph of an Ag interdigital electrode patterned on a convex surface of a Florida fighting conch shell. f) Schematic of a ZnO/Ag sensor. g) *I–V* curves of an ZnO/Ag sensor at various UV light power intensities ranging from 50 to 970 µW cm^{-2}. h) Photocurrents of a ZnO/Ag sensor as a function of UV light power densities at a bias potential of 2 V. i) A photograph of a MoO_2 sensor patterned on a convex surface of a moon snail shell. j) Schematic of a PTS-PANI/MoO_2 sensor. k) Dynamic resistance response of a PTS-PANI/MnO_2 sensor to NH3 at concentrations of 0–400 ppm. l) Resistance changes of a PTS-PANI/MoO_2 sensor as a function of NH_3 concentrations.

and temperature can be well fitted as $\Delta R/R_0 = 0.0539T - 1.638$ (Figure 3d), suggesting a good sensing linearity.

To fabricate a UV sensor, an Ag interdigital electrode with a thickness of 50 µm was first fabricated onto a convex surface of a Florida fighting conch shell (Figure 3e) following by coating of ZnO nanowires on the Ag electrode (ZnO/Ag, Figure 3f; Figure S18, Supporting Information), where Ag is the current collector while ZnO is the UV sensing element.[21] SEM image of ZnO/Ag revealed that ZnO nanowires with a thickness of 4.2 µm was uniformly distributed on the surface of Ag electrode (Figure S19, Supporting Information). Figure 3g shows photocurrent-potential (*I–V*) curves of the ZnO/Ag electrode under the UV irradiation with various power densities (*P*). The linear characteristics of these *I–V* curves can be attributed to the Ohmic contact between the ZnO nanowires and the Ag electrode. When *P* is 50 µW cm^{-2}, the slope of the *I–V* curve was determined to be 0.237. The slope increases with the increase of *P* and reaches 1.921 when *P* is 970 µW cm^{-2}, which can be ascribed to the decrease of resistance caused by the generated charge carriers under the UV irradiation. The relationship between *I* and *P* was investigated via extracting *I* at the applied bias of 2 V from the equation: $I = e^{(0.71\ln(P) - 17.4)}$ with R^2 of 0.99 (Figure 3h). This suggests that the photogeneration efficiency is proportional to the UV light power density, which is an important assurance of outputting a stable electrical signal when ZnO is applied as a UV sensor.[22]

NH_3 detection has attracted much attention in the bioelectronics field since the concentration of NH_3 in the breath or urine can be an early diagnosis of some diseases related to the kidney or liver.[23] Herein, a MoO_2 conductive electrode with a thickness of 127 µm was fabricated on a convex surface of a moon snail (Figure 3i). As one of the well-known transition metal oxides with semi-metallic properties, MoO_2 has shown a great potential for bioelectronics due to its excellent electronic conductivity, chemical, and thermal stability, and biocompatibility.[18] The minimum linewidth of the MoO_2 strips was measured to be 117 µm (Figure S20, Supporting Information). Raman spectra of the fabricated MoO_2 exhibited six characteristic peaks centered at 203, 340, 475, 565, 725, and 920 cm^{-1} (Figure S21, Supporting Information).[24] SEM images showed porous structures of MoO_2 due to the generated gas during the laser processing (Figure S22, Supporting Information). To detect NH_3, *p*-toluene sulfonate hexahydrate-polyaniline (PTS-PANI) was coated onto a MoO_2 electrode (Figure 3j; S23, Supporting Information).[25] Resistance of PTS-PANI increases stepwise as NH_3 concentration increases because PTS-PANI is changing into an insulating state (Figure S24, Supporting Information). This result shows that the PTS-PANI/MoO_2 electrode affords a fast resistance change to NH_3 concentrations in a wide range of 0 to 400 ppm (Figure 3k). Moreover, this response is linear (Figure 3l) and can be fitted to the equation of $\Delta R/R_0 = 0.148 \times c(NH_3) + 1.023$. The results suggest that the device shows good performance as a NH_3 sensor.

A PCB is an important component in an electronic system. Advanced 3D conformable electrical systems typically require a variety of discrete components including microcontrollers, sensors, and passive electrical components. These components are traditionally connected to a circuit using processes such as reflow soldering. However, challenges can arise when this technique is applied to a 3D structure. To tackle this challenge, a system-level demonstration of a 3D conformable circuit on a convex surface of a clam was made in this study (**Figure 4**a,b). The system contains a LED, a voltage divider resistor, a light dependent resistor (LDR), a microcontroller, a miniaturized 3.7 V lithium battery, and an Ag PCB. The Ag PCB was conformably fabricated by the developed 5-axis DFL apparatus. Figure 4c illustrates the working mechanism of this 3D conformable circuit. Change of light intensity is first detected by LDR and converted to digital signal via an analog-digital converter (ADC). The microcontroller outputs signal determining the voltage applied to LED. Conversion of the digital signal to an analog voltage is done by a digital-analog converter (DAC). Simultaneously, the Bluetooth module in the microcontroller communicates with a customized smartphone app for real-time visualizing the voltage changes of LDR. As shown in Figure 4d,e, the brightness of the LED increases when the LDR is covered by a hand and then decreases and recovers to the original state when the hand is moving away (Video S2, Supporting Information). Figure 4f shows a typical voltage change applied to LED. The voltage first increases as the hand moves closer to LDR and decreases immediately after the hand moves away.

The ever-increasing deployment of 3D conformable electronics has witnessed an unprecedented increase in the demand of conformable energy storage devices.[26] To meet such a trend, we fabricated a conformable LIG-based micro-supercapacitor (LIG-MSC) directly on a convex surface of a moon snail using the DFL technique (Figure S25a, Supporting Information). First, a PVDF thin film was cast on the moon snail shell surface followed by the DFL processing to fabricate the LIG interdigital electrode with a thickness of 127 µm. LIG acts as an electrode material due to its high electrical conductivity and high porosity.[11] Then, a polymer electrolyte made of poly(vinyl alcohol) (PVA) and H_2SO_4 was applied to the electrode. Details about the device assembly, testing, and data analysis can be found in Supporting Information. Finally, the electrochemical performance of LIG-MSC was evaluated using cyclic voltammetry (CV) and galvanostatic charge-discharge (GCD) measurements. As shown in figure S25b (Supporting Information), all CV curves of LIG-MSC at various scan rates ranging from 5 to 100 mV s^{-1} exhibit a pseudo-rectangular shape, indicating a good electrical double layer capacitive behavior. The specific area capacitance (C_A) was calculated from the CV curves at various scan rates (Figure S25c, Supporting Information). C_A shows a maximum of 22 mF cm^{-2} at a scan rate of 5 mV s^{-1} and decreases with increase of the scan rate due to decreased adsorption/desorption of electrolyte ions into the electrode at high scan rates. Nevertheless, C_A still maintains a value of 8 mF cm^{-2} at a scan rate of 100 mV s^{-1}. The GCD curves (Figure S25d,e, Supporting Information) show nearly triangular shapes at current densities of 0.05–2 mA cm^{-2}, showing a good capacitive behavior. As shown in C_A calculated from GCD curves (Figure S25f), the LIG-MSC delivers C_A of 10 mF cm^{-2} at I_D of 0.05 mA cm^{-2} and 0.8 mF cm^{-2} when I_D increases to 2 mA cm^{-2}.

To further demonstrate its application in smart home, conformable LIG-based strain sensors were fabricated using the DFL technique on the artificial twigs for indoor ventilation

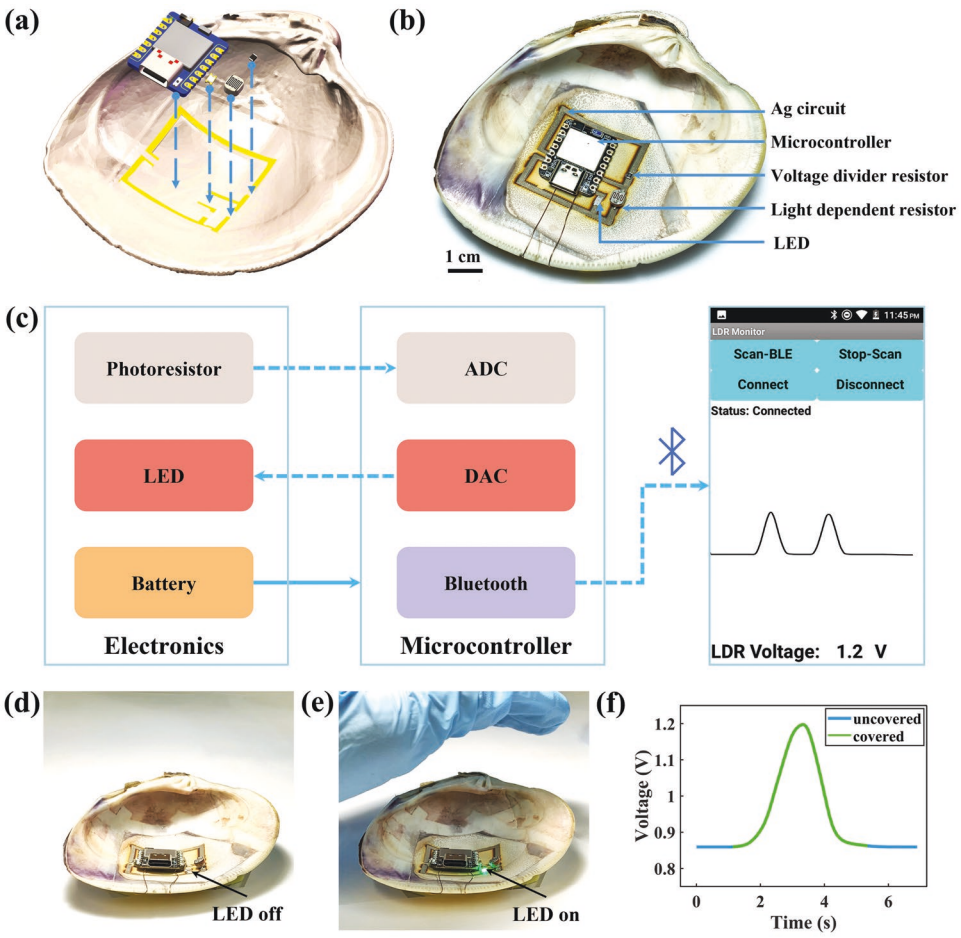

Figure 4. A conformable circuit fabricated on a concave surface of a clam. a) Schematic showing assembly of components for the circuit on a 3D scanned clam model. b) A photograph of the assembled conformable circuit. c) Schematic showing the data flow in the circuit. Photographs show LED being switched off d) and on (e). f) Voltage response of LED when a hand covers on and off LDR.

condition monitoring (**Figure 5**a). Since most daily activities are done indoors, monitoring the environment with a high air quality and a comfort level is very important.[27] A smart appliance that can evaluate indoor ventilation conditions with integrated sensors can help to achieve the goal. Herein, the LIG strain sensors directly fabricated on the artificial twigs can detect wind speed and direction with the aid of the ML algorithms. Swaying of these twigs under the wind leads to change of the strain in LIG, which is reflected in the change ($\Delta R/R_0$) of electrical conductivity of LIG. As illustrated in Figure 5a(i–iii), eight LIG sensors fabricated on the twigs are distributed on an artificial tree in four different directions. Two sensors are placed in each direction at similar heights. This configuration minimizes the number of the sensors without scarifying the measurement accuracy. The collected wind data can be wirelessly transmitted to a computer for data processing and analysis via a pair of radiofrequency modules (Figure S26, Supporting Information).

Response of a LIG strain sensor to various wind speeds was first investigated. Figure 5b shows negative correlation between $\Delta R/R_0$ and wind speeds when the wind blows from the front of the device. It is found that $\Delta R/R_0$ presents piecewise linearity with two different slopes in the region of the wind speed from 3.9 to 5.4m s^{-1} and from 6.5 to 10.58 m s^{-1}. The correlation between $\Delta R/R_0$ and the wind speeds in the two ranges of 3.9–5.4 and 6.5–10.58 m s^{-1} can be well fitted as $\Delta R/R_0 = -0.00393v + 0.000137$ and $\Delta R/R_0 = -0.000765v - 0.0165$, respectively. The decrease of the slope could be due to the nonlinear bending of the twig caused by the increased wind speeds. A comparison between our airflow sensor and those in published works is shown in Table S2 (Supporting Information). After the successful characterization of individual sensors, the spatially resolved sensing is demonstrated in Figure 5c. In the testing, an air circulator fan was placed ≈70 cm away from the tree, which resulted in the wind speeds in the range of 0 ≈3.35 m s^{-1}. A mechanical relay switches the fan periodically on for 2 s and then off for 4 s, leading to a gradually change in the wind speed. This gradual change is reflected on the periodical change of the resistance of the sensors (Figure 5c). Moreover, Figure 5c shows that the LIG strain sensors in the four directions exhibit different $\Delta R/R_0$ values caused by the different bending directions and wind speeds. If the wind bends the twig that compresses the LIG, it causes the denser contact of LIG particles, leading to a negative correlation of $\Delta R/R_0$ and the wind speed.[28] If the bending of the twig causes tension of the LIG, a positive correlation of $\Delta R/R_0$ and the wind speed can be

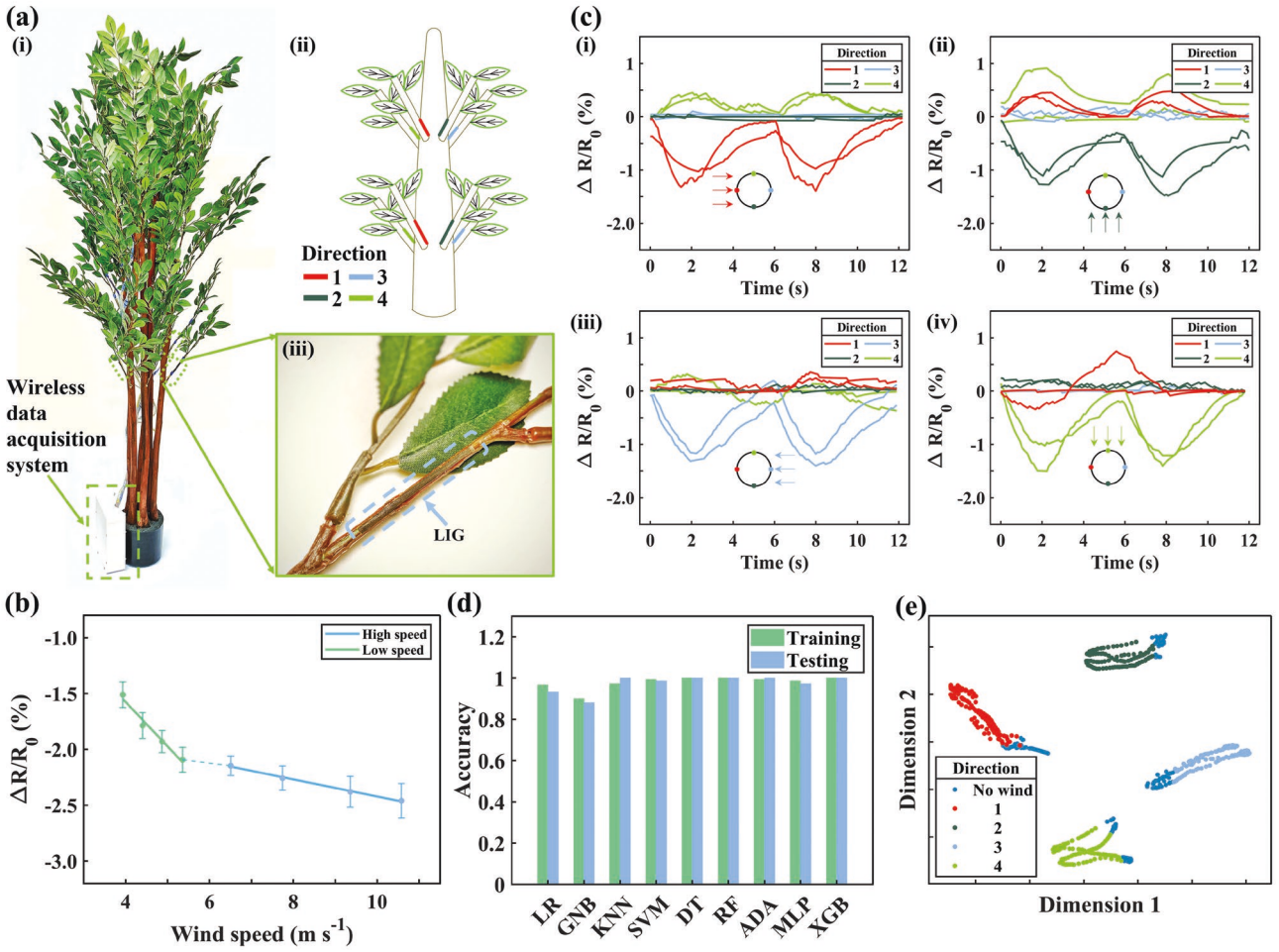

Figure 5. Conformable LIG strain sensors for smart home application. a,i) A photograph of assembled LIG strain sensing system integrated with an artificial tree. ii) Scheme showing distribution of sensors on the tree. iii) A photograph of a LIG sensor on a twig. b) Resistance changes of a single sensor as a function of wind speed. c) Dynamic resistance changes of eight sensors in response to the wind blowing from four directions. d) Training and testing accuracy of nine ML models. e) t-SNE plots of all collected data from the eight sensors tested under the four wind blowing directions.

observed due to increased sparsity of the LIG particles.[29] The sensors which are the closest to the wind source exhibit the biggest changes in $\Delta R/R_0$ at the wind speed reaches the peak. As the distance of the sensors to the wind source increases, $\Delta R/R_0$ decreases as the speed of the wind decreases or wind is blocked by the twigs and leaves. These results imply that through the spatially resolved LIG strain sensors, the wind directions and speeds can be detected in 3D space.

Given the uncertainty and complexity of daily wind conditions, manual analysis of each condition is time- and labor-intensive. Hence, we developed a system that automatically acquires sensing data which is then wirelessly transmitted to a computer for data processing and analysis by the well-trained ML models. A dataset consisting of 900 training and 150 testing sets was collected and labeled to five classes, i.e., no wind, directions of D1, D2, D3, and D4. Nine ML models of Logistic Regression (LR), Gaussian Naïve Bayes (GNB), k-Nearest Neighbors (KNN), Support Vector Machine (SVM), Decision Tree (DT), Random Forest (RF), Adaptive Boosting (ADA), Multilayer perceptron (MLP) and eXtreme Gradient Boosting (XGB) were trained.[30] A 5-fold grid search cross-validation method was conducted to find the optimal hyperparameters (Table S3, Supporting Information). As shown in Figure 5d, all ML models except GNB exhibit training and testing accuracy of >0.93. Among them, DT, RF, and XGB show prediction accuracy of ≈1.0. Table S4 (Supporting Information) shows that their F_1 scores are close to 1.0 except GNB. The confusion matrices of these nine ML models are shown in Figures S27 and S28 (Supporting Information). Among them, DT, RF, and XGB perform the best on the test dataset and afford no false positive and false negative values. These results indicate that the wind directions can be well classified. The workflow of this smart artificial tree for predicting the wind conditions is shown in Video S3 (Supporting Information). To better understand why these models can well classify the wind directions, *t*-distributed stochastic neighbor embedding (*t*-SNE) was employed to reduce the data into two dimensions. Figure 5e shows that the data collected from all sensors under the four different wind directions is clustered into four separate groups. It visually shows that the data in these groups possesses distinguishable characteristics, which is the reason why they could be well classified by the ML models. These results indicate that a conformable sensing

system integrated with home furniture or appliance represents a solid step toward continuous and customized indoor ventilation system monitoring. The technology can be easily extended to other application domains.

3. Conclusion

In this work, we report a new method combining 5-axis laser apparatus with 3D scanning for direct freeform laser fabrication of 3D conformable functional materials on targeted arbitrary surfaces with complex geometries. These functional materials include LIG, metal, and metal oxide. As proof-of-concept demonstrations, 3D conformable electronic devices based on these materials were systematically investigated for applications in temperature/UV light/ammonia sensors, circuit for IoT, energy storage, and strain sensors for smart home. All the sensors exhibit high linearity and accuracy. Moreover, the wireless data transmission and ML algorithms were integrated to further improve the usage of these sensing systems. By integrating these sensors, it can be expected that the seashells can wirelessly transmit the sensed coastal environmental data and that the smart home can improve residents' comfort by dynamically controlling the output of the furniture and appliance.

4. Experimental Section

Chemicals: Polyvinylidene fluoride (PVDF, $M_w = 64.04$ g mol^{-1}, Thermo Fisher Scientific), polyvinyl pyrrolidone (PVP, M_w = 40 000 g mol^{-1}, Sigma–Aldrich), silver nitrate ($AgNO_3$, Fisher), sodium citrate ($Na_3C_6H_5O_7$, Sigma–Aldrich), molybdenum chloride ($MoCl_5$, Fisher), zinc oxide nanowires (ZnO NWs, NWZO01A5, ACS Materials), dimethyl formamide (DMF, Fisher), methanol (Fisher), polyimide films (Dupon), *p*-toluene sulfonate hexahydrate-polyaniline (PTS-PANI, ACS Material), and silver paste (Ted Palla) were used as received without further purification. Deionized water (DI H_2O) was used to prepare the inorganic solution.

Design and Construction of 5-Axis Laser Processing Apparatus: The 5-axis laser platform was built based on a commercial FDM 3D printer (Creality CR-10 V2). The original linear motion mechanism was kept without change. A customized rotational mechanism consisting of two orthogonal direct driven NEMA17 stepper motors, actuated by DRV8825 at 1/32 micro-stepping, were added. The switchable laser module with max power 5 W was directly connected to the C-axis actuator. The control system had been modified with Arduino Mega 2560 R3 and a Ramps 1.6 board. The firmware was updated to an open-source GRBL-MEGA-5X system. An EinScan Pro 2 × 2020 structured light 3D scanner with scanning accuracy of 0.04 mm was used for scanning coordinates of objects.

Fabrication of Ag-based Temperature and UV Sensors: Typically, 0.3 g of sodium citrate and 0.025 g of PVP were dissolved in 10 mL of DI H_2O to form solution A. Meanwhile, 0.52 g of $AgNO_3$ was dissolved in 8 mL of DI H_2O to form solution B. Then, solution B was added drop-by-drop into solution A under stirring. By continuous stirring for 1 h, a silver ink stock solution was obtained. The silver ink precursor was then drop cast evenly on the targeted surfaces and dried in the oven at 40 °C. A Hilbert pattern and an interdigital pattern for temperature sensing were processed by DFL at a scan rate of 500 mm min^{-1} and a laser power of 3.5 W. Then, 30 µL of ZnO nanowires aqueous solution (3 mg mL^{-1}) for the UV light sensing was uniformly drop-coated on the interdigital Ag pattern and dried at the room temperature for 2 h.

To test the temperature sensing performance, the fabricated Ag sensor was placed in the oven whose temperature was varied from 30 to 50 °C at a 2 °C interval. The surface temperature of the sensor was measured by an attached thermometer (HH309A, OMEGA Engineering). The resistance response was measured by a source meter (2604B, Keithley Instruments). At each temperature interval, measurement was taken after the temperature was stabilized. The response of the temperature sensor was calculated using resistance change before and after a temperature change.

To evaluate the UV sensing performance, a UV light source (AI-2UV20DC) was used. To adjust the light intensity, a height-adjustable gantry was used. The UV intensity was determined by a UV Meter (General Tools, UV513AB, 280–400 nm). The sensor was first placed underneath the UV light source. The gantry attached by a UV light source was set at the location that yields a UV intensity of 50 µW cm^{-2}. The resistance response was measured by a source meter (2604B, Keithley Instruments). Afterward, the gantry was lowered to increase the UV light intensity until reaching 970 µW cm^{-2}. Measurement at each UV intensity was taken after the intensity was stabilized. The response of the UV light sensor was characterized by its resistance change.

Fabrication and Testing of MoO_2-based Ammonia Sensors: First, 0.5 g $MoCl_5$ was dissolved in 10 mL ethanol. Then, the $MoCl_5$ solution was spray coated evenly onto the plasma-treated and heated surface of the shell under heating. Then, the predesigned electrode was prepared using the DFL process at a scan rate of 600 mm/min and a laser power of 4.5 W. After electrode fabrication, 30 µL PTS-PANI solution (3 mg mL^{-1}) was drop-coated evenly onto the fabricated electrode and dried at room temperature for 2 h. During the test process, the PTS-PANI coated MoO_2 electrode was properly placed in an acrylic chamber following by injecting specific volumes of NH_3 gases into the chamber using a syringe. A fan was used to speed up gas diffusion. The response of the PTS-PANI coated MoO_2 sensor was calculated using the resistance changes before and after exposure to NH_3 gas. This response was recorded by Keithley 2604B source meter, which was reflected by resistance change of the sensor.

Fabrication and Testing of LIG-based Strain Sensors: Polyimide (PI) sticky tape was attached to the artificial twig. It was then processed by the DFL apparatus at a scan rate of 400 mm min^{-1} and a laser power of 4.5 W. Eight LIG sensors were divided into four groups and placed on an artificial tree in four directions at similar heights rotated at ≈90°. The eight sensors were connected to a multiplexer (CD74HC4067) which ports eight signal channels to an ADC module (ADS1115). After each scanning, the sensed data was transmitted to another microcontroller through a pair of radiofrequency modules. Eventually, the data was input to MATLAB through serial communication. The wind was generated by a vacuum blower (DeWALT DXV10P). The wind speed was quantified by a digital Anemometer (BT-856-A, BTMETER). Characterization of sensors in response to the wind in different directions was performed by placing the wind source in 70 cm distance to the artificial tree. The peak wind speeds were varied by changing the distances. The distance range of 0.3-2.5 m leads to the wind speeds in the range of 3.9–10.58 m s^{-1}.

Materials Characterization: SEM was conducted on ThermoFisher Scientific Volumescope 2 SEM and FEI Quanta 600F to investigate the morphologies of as-prepared samples. Raman spectra were collected on a Renishaw Via Raman spectroscopy.

Machine Learning Algorithms: The data were first processed to the same scale by multiplying the scale factor determined by the channel that presents the largest absolute response, scale_factor = 1/max(abs(eight channel data)). Hence, all data were rescaled to the range of –1–0. The index of the scaled data of two sensors was labeled as "index_with_wind" ($\Delta R/R_0 < -0.3\%$) and "index_no_wind" ($\Delta R/R_0 > 0.3\%$). After that, all sensory data of eight channels was grouped into "with wind" and "no wind" by using the previously obtained two index arrays. The "with wind" group was further labeled into four classes according to the direction of the wind source. Finally, the whole datasets were split into 900 sets and 150 sets for training and testing, respectively, after random shuffling. Nine ML models including LR, GNB, KNN, DT, RF, SVM, MLP, ADB, and XGB were trained. Hyperparameters were optimized through a fivefold grid search cross-validation method (Table S3, Supporting Information).

Supporting Information

Supporting Information is available from the Wiley Online Library or from the author.

Acknowledgements

J.L. thanks the financial support from U.S. National Science Foundation (award number: 1825352 and 1933861) and U.S. Department of The Interior (grant number: R21AC10073-00). Z.Y. acknowledges the financial support from NSF (award number: 2045101).

Conflict of Interest

The authors declare no conflict of interest.

Author Contributions

B.Z. designed and constructed the direct freeform laser processing platform, and he conducted the materials synthesis and characterization as well as the sensor performance test. G.Z. assisted in sensor assembly and test. Y.Z. provided suggestions in sensor design and test. Y.X. offered supervision on material synthesis and characterization, and machine learning algorithm development. J.L. conceived the project, managed the research progress, and provided regular guidance. Y.X. and B.Z. drafted the manuscript which was revised by J.L. All authors agreed to the final version of the manuscript.

Data Availability Statement

All source data and program codes are available from the corresponding author upon reasonable request.

Keywords

3D conformable electronics, direct freeform lasers, machine learning, sensors

Received: August 30, 2022
Revised: October 5, 2022
Published online: October 26, 2022

[1] a) Y. Huang, H. Wu, L. Xiao, Y. Duan, H. Zhu, J. Bian, D. Ye, Z. Yin, *Mater. Horizon.* **2019**, *6*, 642; b) C. Zhang, M. Qu, X. Fu, J. Lin, *Small Methods* **2022**, *6*, 2101384; c) H. Li, Y. Ma, Y. Huang, *Mater. Horizon.* **2021**, *8*, 383; d) H. Wu, Y. Tian, H. Luo, H. Zhu, Y. Duan, Y. Huang, *Adv. Mater. Technol.* **2020**, *5*, 2000093; e) P. Zhu, Y. Wang, Y. Wang, H. Mao, Q. Zhang, Y. Deng, *Adv. Energy Mater.* **2020**, *10*, 2001945; f) Y.-G. Park, G.-Y. Lee, J. Jang, S. M. Yun, E. Kim, J.-U. Park, *Adv. Healthcare Mater.* **2021**, *10*, 2002280.

[2] a) J. A. Paulsen, M. Renn, K. Christenson, R. Plourde, presented at 2012 Future of Instrumentation International Workshop (FIIW) Proceedings, 8–9 Oct. 2012, **2012**; b) G. L. Goh, V. Dikshit, R. Koneru, Z. K. Peh, W. Lu, G. D. Goh, W. Y. Yeong, *The International Journal of Advanced Manufacturing Technology* **2022**, *120*, 2573; c) H. S. An, Y.-G. Park, K. Kim, Y. S. Nam, M. H. Song, J.-U. Park, *Adv. Sci.* **2019**, *6*, 1901603.

[3] Z. Y. Rao, Y. T. Lu, Z. W. Lie, Y. S. Sim, Z. Q. Ma, J. L. Xiao, C. J. Yu, *Nat. Electron.* **2021**, *4*, 513.

[4] S.-J. Oh, T. G. Kim, S.-Y. Kim, Y. Jo, S. S. Lee, K. Kim, B.-H. Ryu, J.-U. Park, Y. Choi, S. Jeong, *Chem. Mater.* **2016**, *28*, 4714.

[5] W. Lee, Y. Liu, Y. Lee, B. K. Sharma, S. M. Shinde, S. D. Kim, K. Nan, Z. Yan, M. Han, Y. Huang, Y. Zhang, J.-H. Ahn, J. A. Rogers, *Nat. Commun.* **2018**, *9*, 1417.

[6] a) A. Carlson, A. M. Bowen, Y. Huang, R. G. Nuzzo, J. A. Rogers, *Adv. Mater.* **2012**, *24*, 5284; b) Z. Rao, Y. Lu, Z. Li, K. Sim, Z. Ma, J. Xiao, C. Yu, *Nat. Electron.* **2021**, *4*, 513; c) K. Sim, F. Ershad, Y. Zhang, P. Yang, H. Shim, Z. Rao, Y. Lu, A. Thukral, A. Elgalad, Y. Xi, B. Tian, D. A. Taylor, C. Yu, *Nat. Electron.* **2020**, *3*, 775; d) M. A. Meitl, Z.-T. Zhu, V. Kumar, K. J. Lee, X. Feng, Y. Y. Huang, I. Adesida, R. G. Nuzzo, J. A. Rogers, *Nat. Mater.* **2006**, *5*, 33; e) D.-H. Kim, N. Lu, R. Ghaffari, Y.-S. Kim, S. P. Lee, L. Xu, J. Wu, R.-H. Kim, J. Song, Z. Liu, J. Viventi, B. de Graff, B. Elolampi, M. Mansour, M. J. Slepian, S. Hwang, J. D. Moss, S.-M. Won, Y. Huang, B. Litt, J. A. Rogers, *Nat. Mater.* **2011**, *10*, 316.

[7] a) J. Choi, C. Han, S. Cho, K. Kim, J. Ahn, D. D. Orbe, I. Cho, Z.-J. Zhao, Y. S. Oh, H. Hong, S. S. Kim, I. Park, *Sci. Adv.* **2021**, *7*, eabj0694; b) K. Wu, Q. Zhou, H. Zou, K. Leng, Y. Zeng, Z. Wu, *Micromachines* **2019**, *10*, 160.

[8] D. Yoo, S. Kim, W. Cho, J. Park, J. Kim, *Small Methods* **2022**, *6*, 2100869.

[9] N. Yi, Y. Gao, A. Lo Verso, J. Zhu, D. Erdely, C. Xue, R. Lavelle, H. Cheng, *Mater. Today* **2021**, *50*, 24.

[10] a) F. Ershad, A. Thukral, J. Yue, P. Comeaux, Y. Lu, H. Shim, K. Sim, N.-I. Kim, Z. Rao, R. Guevara, L. Contreras, F. Pan, Y. Zhang, Y.-S. Guan, P. Yang, X. Wang, P. Wang, X. Wu, C. Yu, *Nat. Commun.* **2020**, *11*, 3823; b) L. M. Ferrari, K. Keller, B. Burtscher, F. Greco, *Multifunct. Mater.* **2020**, *3*, 032003; c) S. Kabiri Ameri, R. Ho, H. Jang, L. Tao, Y. Wang, L. Wang, D. M. Schnyer, D. Akinwande, N. Lu, *ACS Nano* **2017**, *11*, 7634.

[11] J. Lin, Z. Peng, Y. Liu, F. Ruiz-Zepeda, R. Ye, E. L. G. Samuel, M. J. Yacaman, B. I. Yakobson, J. M. Tour, *Nat. Commun.* **2014**, *5*, 5714.

[12] a) B. Sun, R. N. McCay, S. Goswami, Y. Xu, C. Zhang, Y. Ling, J. Lin, Z. Yan, *Adv. Mater.* **2018**, *30*, 1804327; b) L. Huang, J. Su, Y. Song, R. Ye, *Nano-Micro Lett.* **2020**, *12*, 157.

[13] a) Y. Xie, C. Zhang, X. He, T. White, J. D. Demaree, M. Griep, J. Lin, *J. Power Sources* **2018**, *397*, 37; b) R. Ye, Z. Peng, T. Wang, Y. Xu, J. Zhang, Y. Li, L. G. Nilewski, J. Lin, J. M. Tour, *ACS Nano* **2015**, *9*, 9244; c) H. Deng, C. Zhang, Y. Xie, T. Tumlin, L. Giri, S. P. Karna, J. Lin, *J. Mater. Chem. A* **2016**, *4*, 6824.

[14] H. Deng, K. Sattari, Y. Xie, P. Liao, Z. Yan, J. Lin, *Nat. Commun.* **2020**, *11*, 6325.

[15] L. Wu, M. Chen, J. Xu, S. Sun, L. Li, *J. Adv. Manuf. Technol.* **2021**, *114*, 2271.

[16] Y. Xie, C. Zhang, J.-W. Su, H. Deng, C. Zhang, J. Lin, *ChemSusChem* **2019**, *12*, 473.

[17] W. Zhou, S. Bai, Y. Ma, D. Ma, T. Hou, X. Shi, A. Hu, *ACS Appl. Mater. Interfaces* **2016**, *8*, 24887.

[18] G. Zhao, Y. Ling, Y. Su, Z. Chen, C. J. Mathai, O. Emeje, A. Brown, D. R. Alla, J. Huang, C. Kim, Q. Chen, X. He, D. Stalla, Y. Xu, Z. Chen, P.-Y. Chen, S. Gangopadhyay, J. Xie, Z. Yan, *Sci. Adv.* **2022**, *8*, eabp9734.

[19] C. Zhang, H. Deng, Y. Xie, C. Zhang, J.-W. Su, J. Lin, *Small* **2019**, *15*, 1904224.

[20] Q. Li, L.-N. Zhang, X.-M. Tao, X. Ding, *Adv. Healthcare Mater.* **2017**, *6*, 1601371.

[21] Q. Xu, L. Cheng, L. Meng, Z. Wang, S. Bai, X. Tian, X. Jia, Y. Qin, *ACS Appl. Mater. Interfaces* **2019**, *11*, 26127.

[22] A. Wei, L. Pan, W. Huang, *Mater. Sci. Eng. B* **2011**, *176*, 1409.

[23] L. R. Narasimhan, W. Goodman, C. K. N. Patel, *Proc. Natl. Acad. Sci* **2001**, *98*, 4617.
[24] C. Zhang, J. Lu, M. Li, Y. Wang, Z. Zhang, H. Chen, F. Wang, *Green Chem.* **2016**, *18*, 2435.
[25] Z. Ma, P. Chen, W. Cheng, K. Yan, L. Pan, Y. Shi, G. Yu, *Nano Lett.* **2018**, *18*, 4570.
[26] P. Giannakou, M. O. Tas, B. L.e Borgne, M. Shkunov, *ACS Appl. Mater. Interfaces* **2020**, *12*, 8456.
[27] K. Tanaka, S.-H. Yang, Y. Tokudome, Y. Minami, Y. Lu, T. Arie, S. Akita, K. Takei, K. Nakajima, *Adv. Intell. Syst.* **2021**, *3*, 2000174.
[28] L. Chen, M. Weng, P. Zhou, F. Huang, C. Liu, S. Fan, W. Zhang, *Adv. Funct. Mater.* **2019**, *29*, 1806057.
[29] W. Wang, L. Lu, Z. Li, L. Lin, Z. Liang, X. Lu, Y. Xie, *ACS Appl. Mater. Interfaces* **2022**, *14*, 1315.
[30] Y. Xie, C. Zhang, X. Hu, C. Zhang, S. P. Kelley, J. L. Atwood, J. Lin, *J. Am. Chem. Soc.* **2020**, *142*, 1475.